Optimization of the Bulk Heterojunction of All-small-molecule Organic Photovoltaics Using Design of Experiment and Machine Learning Approaches

Aaron Kirkey,[†] Erik J. Luber,[†]* Bing Cao,[†] Brian C. Olsen[†] Jillian M. Buriak[†]*

[†]Department of Chemistry, University of Alberta, 11227-Saskatchewan Drive, Edmonton, AB T6G 2G2, Canada.

ABSTRACT

All-small-molecule organic photovoltaic (OPV) cells based upon the small molecule donor, DRCN5T, and non-fullerene acceptors, ITIC, IT-M, and IT-4F, were optimized using Design of Experiments (DOE) and machine learning (ML) approaches. This combination enables rational sampling of large parameter spaces in a sparse but mathematically deliberate fashion and promises economies of precious resources and time. The work focused upon the optimization of the core layer of the OPV device, the bulk heterojunction (BHJ). Many experimental processing parameters play critical roles in the overall efficiency of a given device and are often correlated, and thus are difficult to parse individually. DOE was applied to the (i) solution concentration of the donor and acceptor ink used for spin-coating, (ii) the donor fraction, and (iii) the temperature and (iv) duration of the annealing of these films. The ML-based approach was then used to derive maps of the PCE landscape for the first and second rounds of optimization to be used as guides to determine the optimal values of experimental processing parameters with respect to device efficiency. This work shows that with little knowledge of a potential combination of components for a given BHJ, a large parameter space can be effectively screened and investigated to rapidly determine its potential for high efficiency OPVs.

Keywords:

organic photovoltaics; Design of Experiments; machine learning, optimization; small-molecules; bulk heterojunction

Graphical Abstract

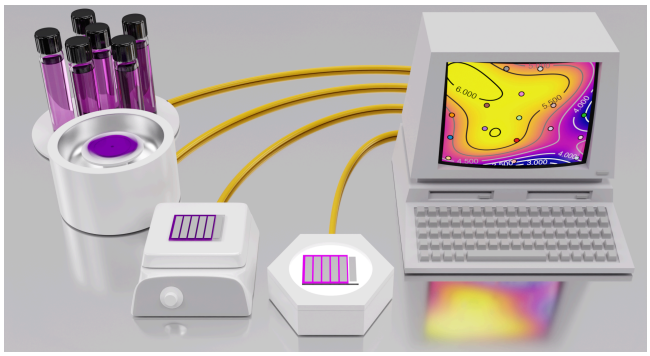

INTRODUCTION

Organic photovoltaics (OPVs) have emerged as a promising class of photovoltaic devices over the past two decades due to ease of manufacturing, inherent flexibility, semi-transparency, and potential for short energy payback times.[1–5] Recently, record power conversion efficiencies (PCE) of 17% for OPVs have been reported,[6–10] reinforcing the viability of these devices as serious contenders for widespread photovoltaic applications. The centerpiece of OPV devices is the bulk heterojunction (BHJ), which consists of donor and acceptor polymers or small molecules. Low bandgap polymers remain the most widely used donor components for producing high-efficiency devices.[11–13] While small-molecule donors have seen less attention compared to low band gap polymers, they possess inherent advantages over polymer donors as they are not subject to batch-to-batch variability of molecular weight and the challenges of purification that are often problematic in polymer syntheses.[14–18] These advantages have underpinned the growth of the literature describing and using these small molecular donors.[19–26] Fullerenes and their derivatives have more recently fallen out of favor due to their weak absorption in the visible range and energy levels that are not easily modulated.[27,28] Efficient non-fullerene acceptors now dominate the recent OPV literature with a growing list of members that includes Y6 and the extensive ITIC family of derivatives.[24,27,29–33] These acceptors offer excellent tunability of absorption properties through well-developed modular organic chemistry.[34,35] The devices optimized in this study contain the donor DRCN5T and one of three acceptors, ITIC, IT-M or IT-4F. These novel all-small-molecule blends leverage the inherent advantages of molecules, they have complementary absorption profiles, and this donor and these acceptors have already shown efficacy in other BHJs.[36–39]

As is the case with all OPVs, the key to efficiency is achieving an ideal nanostructured phase-separated morphology of the BHJ to promote exciton separation and productive harvesting of charge carriers.[29,40,41] Optimizing a new combination of small molecules in a BHJ to form an appropriate morphology has been shown to be particularly challenging.[23,42] The fine balance between competing factors that promote crystallization of both molecular components in the blend, and the kinetics of self-assembly within the film render this process difficult to optimize in a rational and methodical fashion.[19,23,43–49] Many different methods such as thermal annealing,[7,50,51] solvent vapor annealing,[52–54] incorporation of high boiling point additives[55] and combinations thereof,[8,9,56,57] have been used to promote the formation of an ideal nanoscale phase-separated BHJ morphology. As a result of the large number of variables, the parameter space to optimize is wide, particularly with a system that has little in the way of prior investigation.

In spite of the wide range of combinations of processing parameters, BHJs are typically optimized in a one-variable-at-a-time (OVAT) fashion, resulting in lengthy and often incomplete or unsatisfactory device optimization. In addition, the actual process of optimization of OPV devices is often not described in any real detail in the literature, and thus little is known about combinations that did not work. It is therefore difficult to ascertain whether OVAT optimization has indeed led to the “best” possible

performance for a given set and range of variables tested as these parameters are often interconnected and convoluted—varying one could affect others simultaneously.[58] In addition, anthropogenic biases can influence decision-making in a negative manner.[59] An optimization method previously introduced by our research group for OPVs combines Design of Experiment (DOE) and machine learning (ML) approaches to (i) reduce the time required to optimize an OPV system, and (ii) increase the probability of discovering a true optimum.[60] DOE is a rational method that samples large parameter spaces in a sparse but mathematically deliberate fashion that minimizes bias. ML-based algorithms are then combined with the DOE methodology to visually interpret the results and provide guidance for future experimental optimization conditions.

Much of the landscape of the ML literature in the area of OPV uses computational methods to screen candidate molecules for high power conversion efficiencies (PCEs)[61–64] to accelerate materials discovery.[65] In the broader space of materials for clean energy applications, the combining of (sparse) experimental data with ML approaches is growing as the methods become more accessible, widely known and demonstrated. A very recent example is the concept of autonomous self-driving laboratories that perform experimentation *and* analysis, and even suggesting next steps, as shown for thin film materials for perovskite-based PV and other electronic devices.[66] Another example describes the application of a response-surface methodology to tailor the phase and size of Ni_2P nanoparticles, which are used as catalysts for hydrogen evolution reactions.[67] Machine-learning-in-the-loop has been used to optimize the synthesis of PbS colloidal quantum dots for solar cells.[68] An iterative ML approach enabled the optimization of transparent conductive oxides that serve as the basis for OPV and other optoelectronic devices.[69] In terms of method development, Aspuru-Guzik's Phoenics algorithm demonstrates a generalizable Bayesian approach for systems and devices with scant sampling (such as OPV devices) that are "black-box unknown objective functions."[70]

In this article, all-small-molecule OPV devices containing the donor molecule DRCN5T and one of 3 ITIC-based derivatives were optimized using a combination of DOE and ML approaches. This work aims to share the process of exploring the efficacy of the DOE and ML methodology for optimizing new BHJs based upon combinations of small molecules for which scant prior knowledge exists. This combination can be used to examine a large parameter space in an iterative fashion, which is particularly useful when equipped with only sparse antecedent data, if any. The optimization of multiple processing parameters simultaneously, reducing the number of experiments required to investigate such a parameter space to a fraction of what is required for OVAT optimization.

EXPERIMENTAL METHODS

Device Fabrication

The donor and acceptor materials, DRCN5T, ITIC, IT-M and IT-4F were purchased from Ossila, and solvents were purchased from Sigma-Aldrich. All materials and solvents were used as received without further treatment unless otherwise stated. ITO coated glass substrates were purchased from Delta

Technologies (8–12 Ω/sq). ITO glass was sequentially sonicated in dichloromethane, deionized water, and 2-propanol each for 10 min and then dried with an Ar gun (99.998% Ar). The ITO substrates were then cleaned for 10 min in an air plasma with a Harrick plasma cleaner (1.0 torr, PDC 32G, 18W). Zinc acetate dihydrate, ethanolamine and 2-methoxyethanol were purchased from Sigma-Aldrich. ZnO sols were prepared according to prior literature,[71] and the ZnO solution left for 12 hours before the first use. The age of ZnO precursor solution varied from one day to two weeks and within this time frame, no discernible differences in device performance were noted. Both ZnO and BHJ layers were cast using static dispensing from a pipetter with sufficient solution to wet the entire substrate (100 μL), followed by spin-casting. After plasma cleaning, the substrates were again cleaned with a stream of Ar and the ZnO layer was then immediately deposited. 120 μL of ZnO sol was spin-cast in air for 60 s at a spin speed of 4000 rpm and an acceleration of 900 rpm/s. The cast films were then annealed in air at 200 °C for at least 30 minutes.[71] BHJ precursor solutions (chloroform solvent) containing the donor and acceptor components were prepared in an Ar atmosphere glovebox and heated overnight at 40 °C in sealed amber glass vials with a teflon cap. The DRCN5T/ITIC BHJ precursor solutions were formulated from concentrated stock solutions of DRCN5T and ITIC in chloroform and diluted to arrive at chloroform solutions of the desired concentration and donor fraction. The DRCN5T/IT-M and DRCN5T/IT-4F solutions used to fabricate were, however, individually prepared by dissolution in chloroform directly (no stock solutions). Before spin-casting, the chloroform solutions were filtered through a 0.22 μm PTFE filter. BHJ films were prepared by spin-casting 100 μL of BHJ solution at 4000 rpm and an acceleration of 900 rpm/s for 30 s onto Ar-cleaned ZnO-coated ITO sheets and were immediately transferred to a glovebox for thermal annealing in an N_2 atmosphere. Annealing was carried out on a hotplate topped by an aluminum block with a thermocouple insert to ensure accurate temperature and uniform heat distribution. The top electrodes were then deposited as follows: a hole blocking layer of molybdenum oxide (8 nm) and top electrodes comprising Ag (20 nm) and Al (60 nm) were deposited at 0.1, 2.0 and 2.5 Å/s, respectively using thermal evaporation under high-vacuum conditions (~5×10^{-6} Pa). Device areas were 0.155 ± 0.01 cm^2.

Characterization

Thickness measurements of the BHJ films were performed using a Digital Instruments/Veeco multimode AFM in tapping mode and the resulting data were processed using Gwyddion.[72] PV characteristics were measured at ~25 °C in air under AM 1.5G simulated light (Pico Variable LED source from G2V Optics Inc. at 100 mW/cm^2 equivalent intensity from 400 nm to 1100 nm) with a light source calibrated as previously described.[60]

Machine learning approaches

The machine learning algorithm was adapted from Scikit-learn, using a standard scalar and a support vector machine (SVM) using a radial basis function (RBF) kernel with an epsilon of 10^{-5}, a tolerance of 10^{-5}, a regularization parameter (C) of 1.0 and gamma values as indicated in the Supporting Information (table S2).[60]

RESULTS AND DISCUSSION

The OPV devices in this study had an inverted device architecture with ZnO and MoO_x interfacial layers and ITO and Mg/Al as the electrodes, as shown in Figure 1. The BHJs consisted of the small-molecule donor DRCN5T and one of 3 non-fullerene acceptors, ITIC, IT-M or IT-4F. The flatband HOMO and LUMO levels as well as the chemical structures of the donor and acceptor materials are shown in Figure 1.

DOE is more effectively implemented with some preliminary information since the variable space for a new material or device is often so vast—the first step of choosing a starting point may be difficult. Preliminary exploration can provide useful insights into simple questions of solubility of the components being studied, their thermal stability, and other specifics of the system being evaluated. Since little was known of these combinations of compounds for formulating an optimal BHJ, preliminary cells were prepared to evaluate three fundamental parameters: (i) exploration of three chlorinated solvents to determine which, if any, would result in uniform films of the small-molecules comprising the BHJ, (ii) whether thermal annealing was linked to efficiency,[19,73,74] and (iii) a rough range of ratios of the two components in the BHJ that would result in OPVs with efficiencies greater than ~1%. An initial screening of commonly used chlorinated solvents, chloroform, 1,2-dichlorobenzene and chlorobenzene, showed that only layers comprising the components of the BHJ cast from chloroform yielded continuous films when spin-cast onto the ZnO layer, as shown in Figure S2. Thermal annealing was deemed essential as all devices fabricated without thermal annealing had PCEs less than 0.5%. Lastly, BHJs with donor fractions less than 0.5 generally showed low (< 0.5%) power conversion efficiencies, thus providing a lower boundary for optimization. These preliminary exploratory devices also revealed that the BHJ films often appeared non-uniform by visual inspection and were accompanied by particulates and streaks (even with filtration through a 0.22 μm PTFE filter prior to spin-casting); preparation of devices in duplicate was especially important to account for experimental variability.

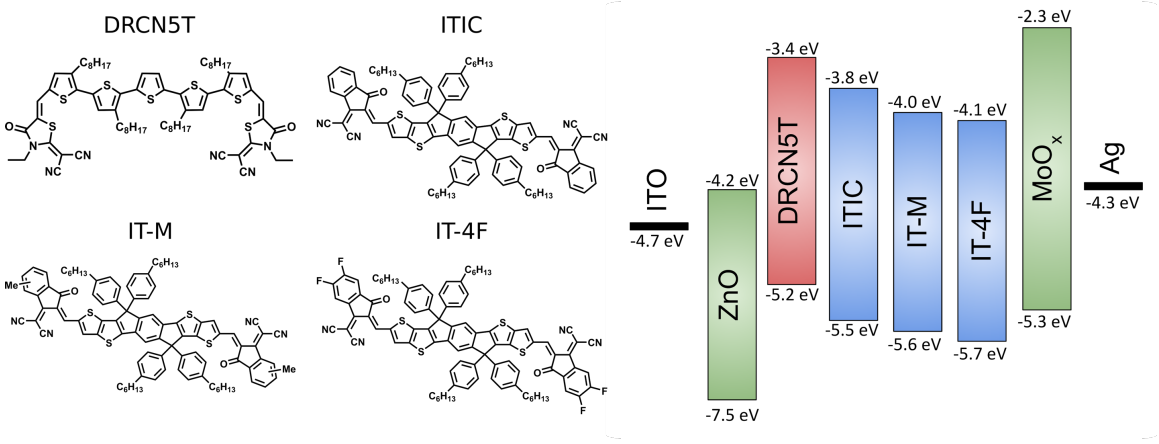

Figure 1. a) Structures of the donor (DRCN5T) and acceptor molecules (ITIC, IT-M and IT-4F), b) OPV device flatband diagram aligned at vacuum level. Values for the HOMO and LUMO levels are derived from the following references: DRCN5T,[36] ITIC,[37] IT-M,[38] IT-4F,[39] and all other materials.[75]

With the preliminary exploration complete, the DOE approach centered on the optimization of 4 BHJ processing parameters: total solution concentration of the donor and acceptor, the ratio of donor:acceptor (represented by the donor fraction), the thermal annealing temperature, and the duration of the thermal annealing. Layer thickness is in part dictated by the viscosity of the BHJ solution used for spin-casting and thus solution concentration is a proxy for layer thickness.[76] Total concentration refers to the total weight of donor and acceptor dissolved in a known volume of chloroform. Donor fraction refers to the weight fraction of the donor material to the total weight of donor and acceptor dissolved in solution.

The goal of the first round of DOE optimization is to sample a parameter space sufficiently wide to try to encompass all performance maxima (in this case, the PCE) within the range of chosen processing parameters. It is not feasible to investigate the entire parameter space of any given system, and larger ranges will require a larger number of levels (sampling points in a range) in order to capture sharper features of the response landscape. If for example, a donor fraction range of 0.1–0.9 is chosen, the number of levels (different values of donor fractions tested) required to attain useful resolution of this parameter range would require a burdensome number of devices. The information presented in Table 1 displays the processing parameters, ranges, and levels investigated in the first round of optimization for the DRCN5T/ITIC BHJ combination. A full factorial design (*i.e.* testing every possible combination of levels for each parameter) of this parameter space would consist of a total of $4^2 \times 3^2 = 144$ experiments/devices. The production of 6-device batches of OPVs, takes ~6 hours in our case, meaning that a full factorial design would require roughly 144 hours of hands-on experimental time. Even without accounting for the necessity of preparing devices in duplicate, this first round of exploratory DOE quickly becomes experimentally prohibitive. Given this fact, the number, range and/or levels of processing parameters could be reduced in order to decrease the number of devices manufactured, or one could apply a different sampling method. Employing the latter, a generalized subset design (GSD) would reduce the DOE array to a more tractable number of experiments, where the number of experiments is reduced by an integer fraction of the full factorial amount.[77] The degree of integer reduction is chosen to be as large as possible while still realizing close to the same number of experiments at each parameter level (See the Supporting Information for a more detailed description of integer reduction).

DRCN5T/ITIC-BASED BHJs

Table 1. Parameters, ranges and levels for the first round of Design of Experiment optimization of DRCN5T/ITIC cells.

BHJ concentrations (mg/ml)	5.0	7.5	10.0	12.5
Number of experiments	4	6	6	4
Donor Fractions	0.6	0.7	0.8	0.9
Number of experiments	4	6	6	4
Annealing Temperatures (°C)	120	140	160	
Number of experiments	7	6	7	

Annealing Time (seconds)	100	200	300
Number of experiments	7	6	7

Through implementation of integer reduction of the DOE array using the GSD algorithm, the total number of experiments was reduced from 144 reduced to 20, with a close to equal number of experiments performed at each different parameter level. A detailed list of each of the parameter levels for each of the 20 experiments can be found in Figure S3. For all experimental conditions, at least two chips comprising 5 cells each (10 cells total) were fabricated and tested.

Before analysis, the data is passed through a filter that excludes non-representative data (statistical outliers) that would otherwise skew the analyses. Devices exhibiting anomalous metrics compared to others made under the same experimental conditions can be systematically identified and excluded according to precise rejection criteria. Examples of devices with anomalous metrics include those with shorts in the device, and thus should be rejected as non-representative. Here we apply a universal rejection of $V_{oc} < 0.65$ V, which is likely to result from a device defect. On average, 8 devices from each experiment will pass the data filter but some combinations of processing parameters lead to devices that are more likely to be rejected. The data that does pass this filter comprises the dataset analyzed in the following steps.

An analysis of variance (ANOVA) is then conducted in order to quantify the relative contribution of each processing parameter.[60] A lower percent contribution means that the processing parameter has little impact, relative to the other parameters within the range tested. The ANOVA in Figure 2 shows the contribution of all 4 processing parameters, total concentration, donor fraction, annealing temperature, and annealing duration on the PCE from the first round of DRCN5T/ITIC optimization. The ANOVA reflects the data acquired from the 20 experiments outlined in Figure S3. Donor fraction and total concentration influence the PCE to the greatest degree over the ranges tested with annealing temperature contributing very little. It is important to note that the small contribution from annealing temperature does not mean that annealing temperature is an insignificant processing parameter, but rather that the range tested was too narrow to have a major effect on performance. Each processing parameter influences PCE as noted by the variance of the J_{sc}, V_{oc}, FF, R_{sh}, or R_{sr} to different degrees; a set of ANOVA for each round of optimization is provided in the Supporting Information, as well as pair plots for each processing parameter and photovoltaic metric (J_{sc}, V_{oc}, *etc.*). A pair plot is simply a scatter plot of any two studied metrics (*e.g.* J_{sc} *vs* total concentration) that can be used to graphically assess any correlations between any two parameters/metrics of interest. The pair plots for every pair of parameters/metrics are shown in Figure S8. From these pair plots, it becomes clear that PCE is most heavily influenced by donor fraction (as previously concluded from the ANOVA). Subplots of Figures S8 e,m show that devices with a donor fraction of 0.8 had dramatically higher PCE and J_{sc} than other donor fractions.

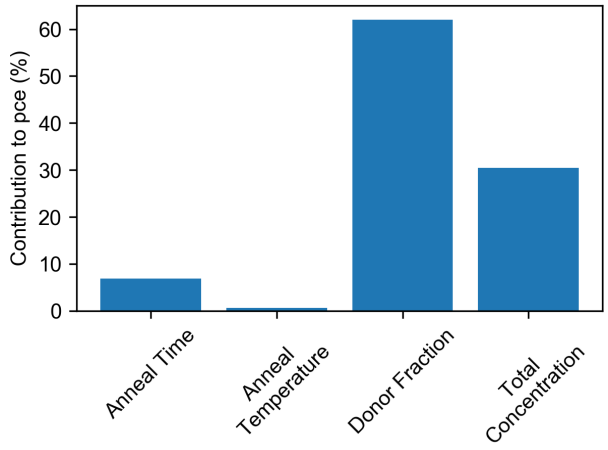

Figure 2. ANOVA plot from the first round of optimization of the BHJ comprising DRN5T/ITIC, revealing the relative contribution of each processing parameter on the resulting PCE. In the range tested, the annealing temperature has little influence on PCE.

The topographic-style maps shown in Figure 3 are a digestible and succinct representation of the data from the experiments outlined in Figure S3, of the first round of DRCN5T/ITIC blend optimization. The maps relate an output (in this case PCE, but in other cases J_{sc} or FF) to the processing parameters. Each data point represents the champion device from every one of the prescribed devices in the experimental list in Figure S3. The entire array of PCE plots for the first round of DRCN5T/ITIC optimization includes all 4 processing parameters. In this figure, within a row, every map has the same annealing duration [*e.g.* maps (a), (b) and (c) contain data points of devices that had annealing durations of 300 s] and within a column, every map has the same annealing temperature [*e.g.* maps (a), (d) and (g) contain data points of devices that were annealed at 120 °C].

As previously mentioned, J_{sc} and PCE are highly correlated and this observation is corroborated by the similarity between the J_{sc} ML maps in Figure S10 and the PCE maps in Figure 3. Devices produced at a total concentration <8 mg/mL displayed relatively low PCE (Figure 3) and J_{sc} (Figure S10), independent of donor concentration and annealing temperature. Films spin-cast from solutions of lower concentrations would be expected to lead to thinner films and thus to lower short-circuit currents as fewer photons can be absorbed.

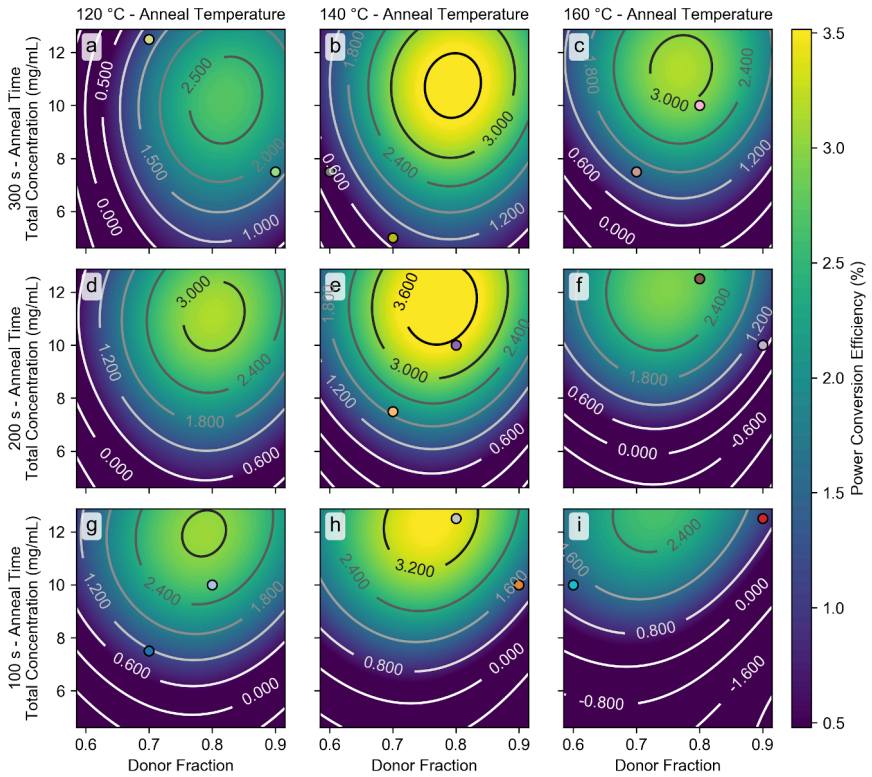

Figure 3. ML-generated PCE maps for the first round of optimization of the DRCN5T/ITIC BHJ devices. This set of maps shows the effect of all four processing parameters on PCE, with areas of higher PCE represented by yellow, and lower by blue.

The most promising region of the parameter space for producing high efficiency devices in Figure 3 is found at total concentrations >10 mg/ml, donor concentrations of ~0.75–0.8, and an annealing temperature of ~140 °C. This information from the first round of optimization was then used to inform the new parameter ranges for the second round of optimization. 4 total concentrations of 8, 11, 14 and 17 mg/mL, 3 donor fractions of 0.65, 0.75, and 0.85, 3 annealing temperatures of 130, 140 and 150 °C, and 3 annealing times of 1.5, 4 and 6.5 min were selected for the second round of optimization. The number of experiments of a full factorial design of 108 was reduced to 20 by using the integer reduction method explained earlier and are enumerated in Figure S3, labelled ITIC Round 2. The corresponding maps for the second round of DRCN5T/ITIC BHJ mixtures are shown below in Figure 4.

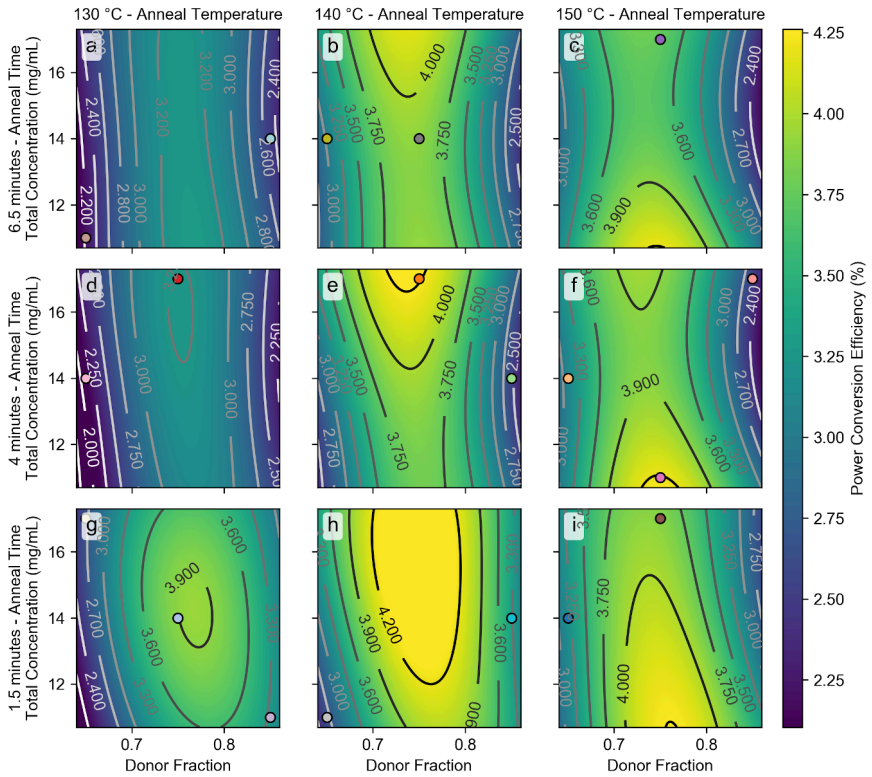

Figure 4. ML-generated PCE maps for the second round of optimization of the devices based on a BHJ composed of DRCN5T/ITIC. These maps are acquired at a higher sampling resolution in a narrower range of parameter space than the first round of optimization, shown in Figure 3.

From the plots in Figure 4, it is clear that the optimum donor fraction appears to be captured within the studied range, suggesting that a maximum PCE is achieved at value of ~0.76. The PCE is influenced dramatically by donor fraction in this round of optimization, and the effect of annealing temperature is small, as shown in Figure S7. The chosen range for the donor fraction in this round of optimization (0.65–0.85) may simply be wider than the other processing parameters. As an extreme example, if a range of annealing temperatures from 10–1000 °C had been chosen, the ANOVA would certainly have shown that temperature would have a much larger effect on PCE than donor fraction; here, such a narrow temperature range would be expected to be less significant. Devices manufactured with a donor fraction of 0.75 displayed the highest PCE and were accompanied by maximization of the J_{sc}, as shown in Figure S9m. PCE varies little across total concentration, annealing temperature, and annealing time, as shown in Figures S9 f,g,h, respectively.

Lastly, it is important to note the sparsity of data points in certain individual maps. When reducing the number of experiments used to explore a parameter space, there is always an inherent trade-off between sampling resolution and number of devices fabricated. Comparing the champion device from the first and second rounds of optimization, the PCE increased from 3.5% to 4.3%, the J_{sc} from 9.2 mA/cm^2 to 10.2 mA/cm^2, V_{oc} from 0.89 V to 0.96 V, while the FF remained unchanged at 0.43. This increase in PCE

from round one to round two of optimization highlights the iterative power of this approach. It allows researchers to narrow ranges of processing parameters or to exclude certain parameters altogether in order to investigate more promising (higher PCE) areas identified in the first round of optimization.

DRCN5T/IT-M-BASED BHJs

The related derivative, IT-M, varies only by the addition of two methyl groups on the extreme ends of the ITIC molecule, and has similar HOMO/LUMO levels to that of the parent ITIC, as shown in Figure 1. As described earlier for the parent ITIC derivative, preliminary screens of DRCN5T/IT-M devices showed that thermal annealing is required to achieve a PCE greater than 0.5%. These tests also showed that at an annealing temperature of 140 °C and increasing annealing time from 8 min to 32 min had no effect on PCE. Device PCEs increased with annealing times up to 8 mins and plateaued. As a result, for the first round of optimization, a fixed annealing time of 8 min was chosen, thereby eliminating time as a variable to optimize. The processing parameters optimized in the first round included (i) BHJ solution total concentration, (ii) BHJ solution donor fraction, and (iii) annealing temperature at a fixed annealing time of 8 min. Having reduced the number of processing parameters from 4 to 3, if each parameter has 3 levels, the full factorial design would have 27 distinct experimental conditions that can be reduced to just 9 experiments using GSD sampling. The table of processing parameters levels for the first round of optimization as well as the experiment list can be found in the Supporting Information, in Figure S16. The resulting PCE maps from the first round of DRCN5T/IT-M optimization along with the corresponding ANOVA plots, are presented below in Figure 5.

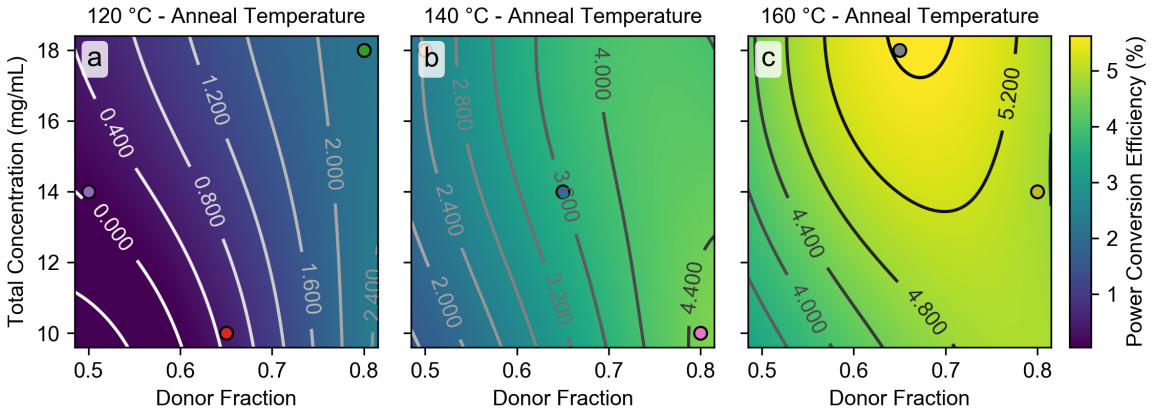

Figure 5. Maps of PCEs as generated *via* ML methods for the first round of optimization for the devices comprising a BHJ of composition of DRCN5T/IT-M. A fixed annealing time of 8 min reduces the dimensionality of this round of optimization to 3 processing parameters, reducing the parameter space and increasing data point density.

The plots in Figures 5a,b,c show the effect of annealing at temperatures of 120, 140 and 160 °C, respectively. Scanning the plots from left to right reveals that devices annealed at higher temperatures exhibit higher PCEs. This observation is corroborated by the ANOVA for PCE in Figure S21, which

highlights the contribution that annealing temperature plays on the PCE. The linkage between temperature and PCE is the focus of the next round of optimization. Annealing devices at 160 °C increased the PCE primarily through an increase in the FF of Figure S26b. Given the shallower LUMO level of IT-M (-3.98 eV),[38] compared to ITIC (-3.83 eV),[37] the observed decrease in V_{oc} shown in Figure S27 is expected.[78,79] As shown in Figure S20, the total concentration of the BHJ solutions influences PCE and J_{sc} very little and as such the range was extended substantially for the second round of optimization.

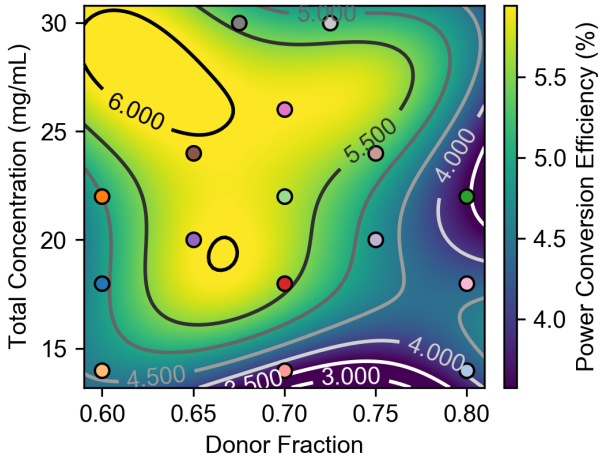

Figure 6. Maps of PCEs as generated *via* ML methods for the second round of optimization of DRCN5T/IT-M-based devices. An optimal annealing temperature of 160 °C was identified, leaving two processing parameters to optimize, the donor fraction and total concentration.

In the second round of optimization of the DRCN5T/IT-M combination, higher annealing temperatures of 160, 180 and 200 °C were chosen, as well as a narrower range of BHJ solution donor fractions of 0.6, 0.7 and 0.8. With 3 levels per parameters, this yields a full factorial design of 27 unique experimental conditions that were reduced to just 9 after GSD integer reduction. The table of processing parameters for the second round of optimization and corresponding list of experiments can be found in the Supporting Information, figure S16. Devices annealed at 200 °C had substantially lowered V_{oc}s, dropping from roughly 0.9 V to values ranging from 0.7–0.2 V. Figure S18a shows the distribution of PCEs for devices made under each set of experimental conditions; experimental labels match those assigned in Figure S16 for round 2. Figure S18c displays the number of devices from each experimental condition to pass the data filter; it shows that devices that were annealed at 200 °C were all rejected by the data filter based on low V_{oc}s (experiment #2, #6 and #8). While it is important to include data from devices with high and low PCEs, it seems that annealing at 200 °C is detrimental. In some instances, devices annealed at 180 °C also showed drops in V_{oc} of up to 0.3 V, and most devices annealed at 180 °C had lower PCEs than those annealed at 160 °C, as shown in Figure S23g. At this point, instead of continuing forward as planned, devices annealed at 180 and 200 °C were omitted from this analysis as focusing on devices annealed at 160 °C seemed more fruitful, providing more consistent and reproducible results.

The experiments originally designated to be annealed at 180 or 200 °C, as per the generated list in Figure S16, were instead run at 160 °C. The resulting map can be found in the Supporting Information as Figure S28. This map contains some high PCE features that were deemed worthy of further exploring. As a result, specific devices were prepared in order to increase the density of data points in this promising parameter space. The map derived from this more granular data for the DRCN5T/IT-M BHJ composition is shown in Figure 6, and it shows a rather flat PCE landscape. In the range tested, the total solution concentration of BHJ components and the donor fraction had equal contributions on the resulting PCE, as shown in PCE ANOVA in Figure S21. PCE did not vary with a total concentration of 20-26 mg/mL and donor fractions of 0.65–0.70. After this second round of optimization, the champion device had a PCE of 5.9%, J_{sc} = 12.2 mA/cm^2, FF = 0.53 and a V_{oc} = 0.93 V. This champion device shows little improvement from the first round of DRCN5T/IT-M optimization whose champion had a PCE of 5.7%. The fact that no further improvement in PCE was noted in generation two suggests that a maximum has been reached and that further optimization of these parameters will probably not be fruitful, which is useful information.

DRCN5T/IT-4F-BASED BHJs

The IT-4F derivative has two pairs of fluorines on the extreme ends of the ITIC molecule, further lowering the HOMO and LUMO levels compared to the two acceptors described thus far. Preliminary devices demonstrated the need to optimize all 4 processing parameters. Three levels were chosen for every parameter except for annealing temperature where two levels were chosen. This yields 81 possible combinations that were reduced using GSD sampling to a list of 13 experiments, that can be found in figure S32. Based upon the results with ITIC and IT-M, narrower windows of BHJ solution donor fraction (0.6–0.8) and annealing temperatures (150 and 170 °C) were chosen. Figure 7 below displays the results from the first round of optimization.

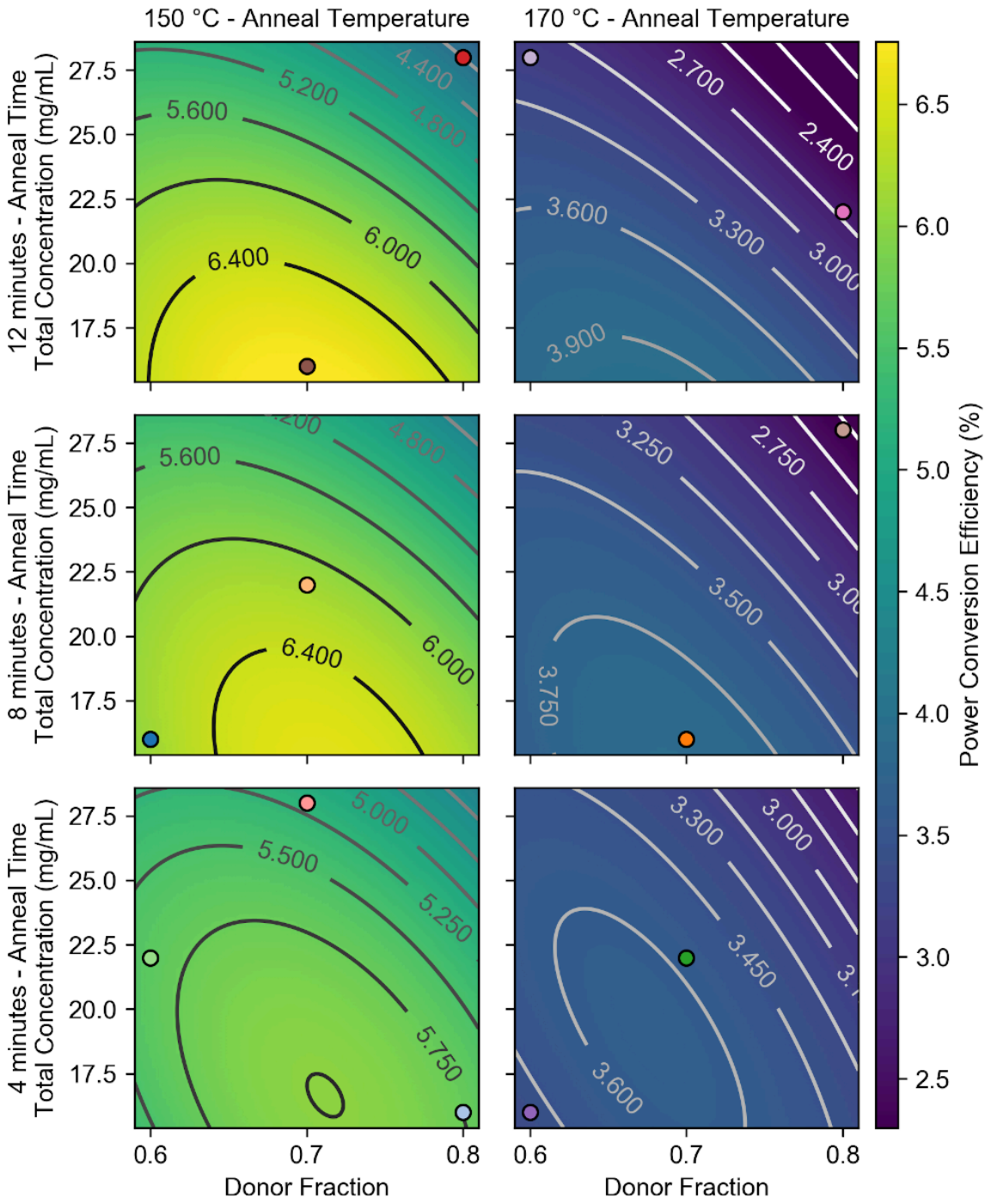

Figure 7. Maps of PCEs as generated *via* ML methods for the first round of optimization of the devices with BHJs comprising DRCN5T/IT-4F. This set of maps shows the effect of all 4 processing parameters on PCE, with higher areas of PCE represented by yellow, and lower by blue.

Comparing the columns of subplots in Figure 7, devices annealed at 150 °C exhibit substantially higher PCEs than devices annealed at 170 °C. This finding is corroborated by the pair plots in Figure S37. The maps in Figure S39 display similar topologies, suggesting that an increased J_{sc} for devices annealed at

150 °C is the main driver of increased PCE. Figure S33a shows that annealing temperature most heavily influences PCE within this range.

Devices prepared with lower total concentrations (representing the bottom half of each map in Figure 7) exhibited higher PCEs. Figured S37 f,h demonstrate that lower total concentrations and longer annealing times result in devices with higher PCE. The device with the highest PCE (experiment #11 figure S32) had a BHJ solution concentration and donor fraction of 16 mg/mL and 0.7, respectively, and was annealed at 150 °C for 12 min. The distribution of PCEs varies little with different donor fractions (figure S37e) and as a result, a fixed donor fraction of 0.7 was chosen for all devices in the second round of optimization.

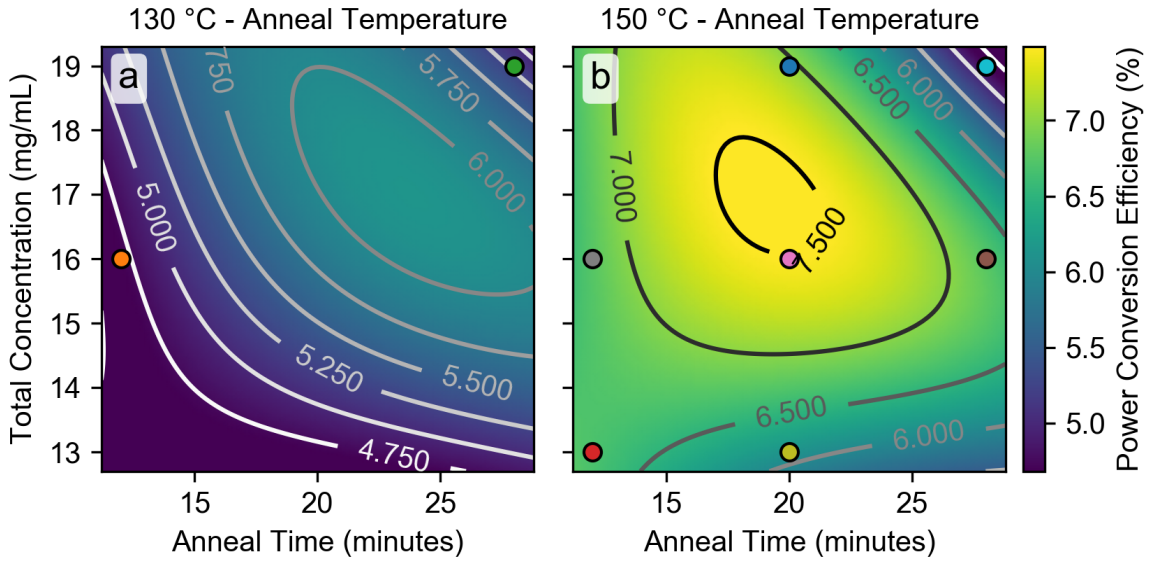

Figure 8. ML-generated PCE maps for the second round of optimization of devices with BHJs comprising DRCN5T/IT-4F BHJ. This set of maps shows the effect of all 4 processing parameters on PCE with higher PCE areas represented by yellow and lower PCE by blue.

For the second round of optimization, annealing temperatures of 130 and 150 °C, total concentrations of the BHJ solutions of 13, 16 and 19 mg/mL, and longer annealing times of 12, 20 and 28 min, were chosen. GSD sampling enabled a reduction of experimental conditions to a list of 6 experiments, which are outlined in Figure S32, titled Round 2. The resulting PCE maps are presented in Figure 8. Since the BHJ solution donor fraction was not optimized in this round, the axes for these maps are different from the earlier maps. The x- and y-axes of each plot correspond to annealing temperature and total concentration of the BHJ precursor solution, respectively. The plots differ in their annealing times, as indicated on each panel. Comparing the two plots in Figure 8, it is clear that annealing devices at 150 °C resulted in higher efficiency devices than annealing at 130 °C. The ANOVA in Figure S34 labelled PCE shows that annealing temperature indeed has the largest effect on the PCEs, followed by annealing time, and finally by the total concentration of the BHJ solution. Figures S3 8e,g show that both annealing time

and total concentration had little effect on the PCE over the ranges tested. Interestingly, an annealing temperature of 150 °C seems required in order to achieve a high shunt resistance in these parameter ranges (Figure S34 R_{sh}). A similar effect was found for non-optimal donor fractions in the first round of ITIC device optimization (Figure S6R_{sh}). The second round of IT-4F optimization yielded the best performing device in this study with a PCE = 7.5%, J_{sc} = 15.2 mA/cm^2, FF = 0.62 and a V_{oc} = 0.80 V.

WHAT WAS LEARNED ABOUT OPTIMIZATION OF OPVS COMPRISING THESE 3 ITIC DERIVATIVES?

All three of the ITIC derivative-based BHJs exhibited the highest observed performance with a donor-rich BHJ, in the range of 0.7–0.8. It is possible that without a systematic screening process that allows for the exploration of such large parameter spaces, the compositions of BHJs might have been too narrow to have found the islands of higher PCEs greater than a few percent. It has been reported that the donor molecule DRCN5T readily crystallizes upon annealing at 120 °C, which is thought to promote phase segregation and the formation of percolated pathways.[36] ITIC, on the other hand, requires higher temperatures to induce crystallization,[80] and thus higher ideal annealing temperatures, in the range of 160 °C, are considered essential for optimum performance (Table S1).[81] A compromise would be needed when combining these two components, and thus the optimal annealing conditions would be difficult to predict. The identification of different conditions to arrive at optimal performance of these three combinations of BHJs highlights the lack of generality when one embarks upon the optimization of a new BHJ, even when the molecules are structurally related.

Table 2. Photovoltaic metrics of champion devices after 2 rounds of optimization. Average PCE values and standard deviation in brackets. Averages based on 10, 43 and 35 devices for ITIC, IT-M and IT-4F, respectively.

Acceptor Molecule	PCE (%)	J_{sc} (mA/cm^2)	FF	V_{oc} (V)
ITIC	4.3 (3.9 ± 0.39)	10.3 (9.9 ± 0.48)	0.43 (0.42 ± 0.022)	0.96 (0.94 ± 0.012)
IT-M	5.9 (5.4 ± 0.69)	12.2 (11.5 ± 0.77)	0.53 (0.50 ± 0.043)	0.93 (0.92 ± 0.024)
IT-4F	7.5 (6.2 ± 0.85)	15.2 (13.5 ± 0.78)	0.62 (0.58 ± 0.049)	0.80 (0.78 ± 0.016)

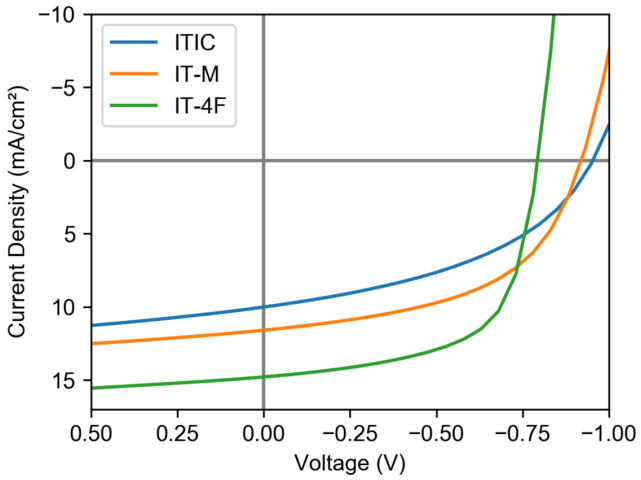

Figure 9. JV curves of the champion devices for all 3 small-molecule donors that were investigated in this work, ITIC, IT-M, and IT-4F, with the donor DRCN5T. The experimental conditions used to fabricate these champion devices were identified after two rounds of the DOE and ML optimization for each composition.

As expected from their previously measured LUMO levels,[37–39] the V_{oc} values of champion devices decrease in the order of ITIC (~0.98 V) > IT-M (~ 0.93 V) > IT-4F (~0.80 V). This admittedly small dataset seems to suggest a trade-off between V_{oc} and J_{sc} and FF; similar trade-offs have been previously identified with other small-molecule acceptors by Cheyns *et al.*[79] Additionally, Ma *et al.* found that matching the crystallinity of the donor and acceptor polymers improved device efficiency,[82] and the same phenomenon is likely to hold for small-molecule OPVs as well.

Given that we have very little in the way of mechanistic rationale to link processing parameters with device properties, it is very difficult to know *a priori* what ranges of parameters could lead to the highest device parameters, especially since there is often a non-linear output from a set of multi-dimensional input parameters that have varying degrees of correlation. Moreover, despite small changes in the donor molecular structure, the range of optimal processing conditions changes in unpredictable ways given that these factors are so intertwined and convoluted. These conclusions highlight one of the strengths of this approach to device optimization: while traditional methods typically sample only a handful of parameters over smaller ranges and test these parameters independently, the DOE-based analyses enable investigation of a broad swath of variables, enabling rational exploration of novel systems with only scant prior knowledge.

CONCLUSIONS

A combination of Design of Experiments- and machine learning-based approaches was used to optimize all-small-molecule devices with the donor DRCN5T and one of the 3 non-fullerene acceptors, ITIC, IT-M, and IT-4F. The effects of donor fraction, BHJ solution concentration, thermal annealing time, and temperature on device performance were elucidated. DOE+ML enabled the investigation of large parameter

spaces while manufacturing significantly fewer devices than a traditional one-variable-at-a-time optimization procedure. As a result, multiple processing parameters were optimized simultaneously, producing a multi-variable dataset that was analyzed by a ML algorithm. The relationship of each processing parameter to PCE was elucidated and topographical maps were produced to visualize the relationships to PCE. No prior information of these novel donor/acceptor mixtures was available and thus preliminary devices proved crucial for identifying processing parameters and their ranges. A data filter was required to handle non-representative data from devices exhibiting physical defects that led to electrical shorts. Two rounds of optimization were conducted for each mixture which allowed for the identification and subsequent exclusion of processing parameters that contributed little to PCE. Additionally in the second round of optimization for each mixture, parameter ranges were narrowed which constricts the parameter space and increases data point density in the regions containing the highest PCE devices.

ASSOCIATED CONTENT

Supporting Information

GSD (generalized subset design)-reduced experimental lists for optimization of each round of all 3 BHJ mixtures, data filter rejection results, ML generated maps for PCE, J_{sc}, FF, and V_{oc} for all rounds of optimization, ANOVAs demonstrating the contribution of PCE, J_{sc}, FF and V_{oc} for all rounds of optimization, pair plot arrays showing the relation of processing parameters to a series of performance metrics for each round of optimization for each mixture and goodness of fit plots for the topographical ML generated maps. This supporting information is available online at the ACS Publications website.

Financial Interests

The authors declare no competing financial interests

AUTHOR INFORMATION

Corresponding Authors

Erik J. Luber - *Department of Chemistry, University of Alberta, Edmonton, AB T6G 2G2, Canada;*
ORCID: 0000-0003-1623-0102
Email: eluber@ualberta.ca

Jillian M. Buriak - *Department of Chemistry, University of Alberta, Edmonton, AB T6G 2G2, Canada;*
ORCID: 0000-0002-9567-4328
Email: jburiak@ualberta.ca

Authors

Aaron Kirkey - *Department of Chemistry, University of Alberta, Edmonton, AB T6G 2G2, Canada;* ORCID: 0000-0002-2835-5060

Bing Cao - *Department of Chemistry, University of Alberta, Edmonton, AB T6G 2G2, Canada;* ORCID: 0000-0002-3825-4669

Brian C. Olsen - *Department of Chemistry, University of Alberta, Edmonton, AB T6G 2G2, Canada;* ORCID: 0000-0001-9758-3641

ACKNOWLEDGMENTS

This work was supported by Future Energy Systems of the University of Alberta (https://futureenergysystems.ca; grant numbers T12-P04 and T12-P01), the Natural Sciences and Engineering Research Council (NSERC, grant number RGPIN-2018-04294), Alberta Innovates Technology Futures (grant numbers AITF iCORE IC50-T1 G2013000198 and CTDP-G2018000919 and funding for A.K. *via* the Alberta Innovates Graduate Student Scholarship), Alberta Innovates and the Canada Research Chairs program (CRC 207142). A.K. thanks the University of Alberta for a QEII Scholarship, Alberta Innovates Technology Futures for a graduate scholarship, the Alberta/Technical University of Munich International Graduate School for Hybrid Functional Materials (ATUMS) program, and MITACS (Globalink research award) for funding. The National Research Council is thanked for the use of facilities at the NRC Nanotechnology Research Centre in Edmonton.

REFERENCES

(1) dos Reis Benatto, G. A.; Roth, B.; Corazza, M.; Søndergaard, R. R.; Gevorgyan, S. A.; Jørgensen, M.; Krebs, F. C. Roll-to-Roll Printed Silver Nanowires for Increased Stability of Flexible ITO-Free Organic Solar Cell Modules. *Nanoscale* **2016**, *8*, 318–326.

(2) Cheng, P.; Li, G.; Zhan, X.; Yang, Y. Next-Generation Organic Photovoltaics Based on Non-Fullerene Acceptors. *Nat. Photonics* **2018**, *12*, 131–142.

(3) Wang, H.; Cao, J.; Yu, J.; Zhang, Z.; Geng, R.; Yang, L.; Tang, W. Molecular Engineering of Central Fused-Ring Cores of Non-Fullerene Acceptors for High-Efficiency Organic Solar Cells. *J. Mater. Chem. A* **2019**, *7*, 4313–4333.

(4) Brus, V. V.; Lee, J.; Luginbuhl, B. R.; Ko, S.-J.; Bazan, G. C.; Nguyen, T.-Q. Solution-Processed Semitransparent Organic Photovoltaics: From Molecular Design to Device Performance. *Adv. Mater.* **2019**, *31*, 1900904.

(5) Bihar, E.; Corzo, D.; Hidalgo, T. C.; Rosas-Villalva, D.; Salama, K. N.; Inal, S.; Baran, D. Fully Inkjet-Printed, Ultrathin and Conformable Organic Photovoltaics as Power Source Based on Cross-Linked PEDOT:PSS Electrodes. *Adv. Mater. Technol.* **2020**, *5*, 2000226.

(6) Meng, L.; Zhang, Y.; Wan, X.; Li, C.; Zhang, X.; Wang, Y.; Ke, X.; Xiao, Z.; Ding, L.; Xia, R.; Yip, H.-L.; Cao, Y.; Chen, Y. Organic and Solution-Processed Tandem Solar Cells with 17.3% Efficiency. *Science* **2018**, eaat2612.

(7) Zhu, L.; Zhang, M.; Zhou, G.; Hao, T.; Xu, J.; Wang, J.; Qiu, C.; Prine, N.; Ali, J.; Feng, W.; Gu, X.; Ma, Z.; Tang, Z.; Zhu, H.; Ying, L.; Zhang, Y.; Liu, F. Efficient Organic Solar Cell with 16.88% Efficiency Enabled by Refined Acceptor Crystallization and Morphology with Improved Charge Transfer and Transport Properties. *Adv. Energy Mater.* **2020**, *10*, 1904234.

(8) Du, X.; Yuan, Y.; Zhou, L.; Lin, H.; Zheng, C.; Luo, J.; Chen, Z.; Tao, S.; Liao, L.-S. Delayed Fluorescence Emitter Enables Near 17% Efficiency Ternary Organic Solar Cells with Enhanced Storage Stability and Reduced Recombination Energy Loss. *Adv. Funct. Mater.* **2020**, *30*, 1909837.

(9) Zhan, L.; Li, S.; Lau, T.-K.; Cui, Y.; Lu, X.; Shi, M.; Li, C.-Z.; Li, H.; Hou, J.; Chen, H. Over 17% Efficiency Ternary Organic Solar Cells Enabled by Two Non-Fullerene Acceptors Working in an Alloy-Like Model. *Energy Environ. Sci.* **2020**, *13*, 635–645.

(10) Lin, Y.; Adilbekova, B.; Firdaus, Y.; Yengel, E.; Faber, H.; Sajjad, M.; Zheng, X.; Yarali, E.; Seitkhan, A.; Bakr, O. M.; El-Labban, A.; Schwingenschlögl, U.; Tung, V.; McCulloch, I.; Laquai, F.; Anthopoulos, T. D. 17% Efficient Organic Solar Cells Based on Liquid Exfoliated WS2 as a Replacement for PEDOT:PSS. *Adv. Mater.* **2019**, *31*, 1902965.

(11) Zhang, W.; Huang, J.; Xu, J.; Han, M.; Su, D.; Wu, N.; Zhang, C.; Xu, A.; Zhan, C. Phthalimide Polymer Donor Guests Enable over 17% Efficient Organic Solar Cells via Parallel-Like Ternary and Quaternary Strategies. *Adv. Energy Mater.* **2020**, *n/a*, 2001436.

(12) Fan, B.; Zhang, D.; Li, M.; Zhong, W.; Zeng, Z.; Ying, L.; Huang, F.; Cao, Y. Achieving over 16% Efficiency for Single-Junction Organic Solar Cells. *Sci. China Chem.* **2019**, *62*, 746–752.

(13) An, C.; Zheng, Z.; Hou, J. Recent Progress in Wide Bandgap Conjugated Polymer Donors for High-Performance Nonfullerene Organic Photovoltaics. *Chem. Commun.* **2020**, *56*, 4750–4760.

(14) Walker, B.; Tamayo, A. B.; Dang, X.-D.; Zalar, P.; Seo, J. H.; Garcia, A.; Tantiwiwat, M.; Nguyen, T.-Q. Nanoscale Phase Separation and High Photovoltaic Efficiency in Solution-Processed, Small-Molecule Bulk Heterojunction Solar Cells. *Adv. Funct. Mater.* **2009**, *19*, 3063–3069.

(15) Bura, T.; Beaupré, S.; Légaré, M.-A.; Quinn, J.; Rochette, E.; Terence Blaskovits, J.; Fontaine, F.-G.; Pron, A.; Li, Y.; Leclerc, M. Direct Heteroarylation Polymerization: Guidelines for Defect-Free Conjugated Polymers. *Chem. Sci.* **2017**, *8*, 3913–3925.

(16) Huo, Y.; Gong, X.-T.; Lau, T.-K.; Xiao, T.; Yan, C.; Lu, X.; Lu, G.; Zhan, X.; Zhang, H.-L. Dual-Accepting-Unit Design of Donor Material for All-Small-Molecule Organic Solar Cells with Efficiency Approaching 11%. *Chem. Mater.* **2018**, *30*, 8661–8668.

(17) Babics, M.; Liang, R.-Z.; Wang, K.; Cruciani, F.; Kan, Z.; Wohlfahrt, M.; Tang, M.-C.; Laquai, F.; Beaujuge, P. M. Solvent Vapor Annealing-Mediated Crystallization Directs Charge Generation, Recombination and Extraction in BHJ Solar Cells. *Chem. Mater.* **2018**, *30*, 789–798.

(18) Wadsworth, A.; Moser, M.; Marks, A.; S. Little, M.; Gasparini, N.; J. Brabec, C.; Baran, D.; McCulloch, I. Critical Review of the Molecular Design Progress in Non-Fullerene Electron Acceptors Towards Commercially Viable Organic Solar Cells. *Chem. Soc. Rev.* **2019**, *48*, 1596–1625.

(19) Zhou, R.; Jiang, Z.; Yang, C.; Yu, J.; Feng, J.; Adil, M. A.; Deng, D.; Zou, W.; Zhang, J.; Lu, K.; Ma, W.; Gao, F.; Wei, Z. All-Small-Molecule Organic Solar Cells with over 14% Efficiency by Optimizing Hierarchical Morphologies. *Nat. Commun.* **2019**, *10*, 5393.

(20) Zhou, Z.; Xu, S.; Song, J.; Jin, Y.; Yue, Q.; Qian, Y.; Liu, F.; Zhang, F.; Zhu, X. High-Efficiency Small-Molecule Ternary Solar Cells with a Hierarchical Morphology Enabled by Synergizing Fullerene and Non-Fullerene Acceptors. *Nat. Energy* **2018**, *3*, 952–959.

(21) Bin, H.; Yao, J.; Yang, Y.; Angunawela, I.; Sun, C.; Gao, L.; Ye, L.; Qiu, B.; Xue, L.; Zhu, C.; Yang, C.; Zhang, Z.-G.; Ade, H.; Li, Y. High-Efficiency All-Small-Molecule Organic Solar Cells Based on an Organic Molecule Donor with Alkylsilyl-Thienyl Conjugated Side Chains. *Adv. Mater.* **2018**, *30*, 1706361.

(22) Guo, J.; Bin, H.; Wang, W.; Chen, B.; Guo, J.; Sun, R.; Zhang, Z.-G.; Jiao, X.; Li, Y.; Min, J. All-Small Molecule Solar Cells Based on Donor Molecule Optimization with Highly Enhanced Efficiency and Stability. *J. Mater. Chem. A* **2018**, *6*, 15675–15683.

(23) Chen, H.; Hu, D.; Yang, Q.; Gao, J.; Fu, J.; Yang, K.; He, H.; Chen, S.; Kan, Z.; Duan, T.; Yang, C.; Ouyang, J.; Xiao, Z.; Sun, K.; Lu, S. All-Small-Molecule Organic Solar Cells with an Ordered Liquid Crystalline Donor. *Joule* **2019**, *3*, 3034–3047.

(24) Huo, Y.; Zhang, H.-L.; Zhan, X. Nonfullerene All-Small-Molecule Organic Solar Cells. *ACS Energy Lett.* **2019**, *4*, 1241–1250.

(25) Cai, F.; Peng, H.; Chen, H.; Yuan, J.; Hai, J.; Lau, T.-K.; Wang, J.; Hu, Y.; Liu, W.; Lu, X.; Zou, Y. An Asymmetric Small Molecule Acceptor for Organic Solar Cells with a Short Circuit Current Density over 24 mA Cm−2. *J. Mater. Chem. A* **2020**, *8*, 15984–15991.

(26) Luo, Z.; Ma, R.; Xiao, Y.; Liu, T.; Sun, H.; Su, M.; Guo, Q.; Li, G.; Gao, W.; Chen, Y.; Zou, Y.; Guo, X.; Zhang, M.; Lu, X.; Yan, H.; Yang, C. Conformation-Tuning Effect of Asymmetric Small Molecule Acceptors on Molecular Packing, Interaction, and Photovoltaic Performance. *Small* **2020**, *16*, 2001942.

(27) Zhang, G.; Zhao, J.; Chow, P. C. Y.; Jiang, K.; Zhang, J.; Zhu, Z.; Zhang, J.; Huang, F.; Yan, H. Nonfullerene Acceptor Molecules for Bulk Heterojunction Organic Solar Cells. *Chem. Rev.* **2018**, *118*, 3447–3507.

(28) Yu, Z.-P.; Liu, Z.-X.; Chen, F.-X.; Qin, R.; Lau, T.-K.; Yin, J.-L.; Kong, X.; Lu, X.; Shi, M.; Li, C.-Z.; Chen, H. Simple Non-Fused Electron Acceptors for Efficient and Stable Organic Solar Cells. *Nat. Commun.* **2019**, *10*, 2152.

(29) Li, S.; Li, C.-Z.; Shi, M.; Chen, H. New Phase for Organic Solar Cell Research: Emergence of Y-Series Electron Acceptors and Their Perspectives. *ACS Energy Lett.* **2020**, *5*, 1554–1567.

(30) McAfee, S. M.; Welch, G. C. Development of Organic Dye-Based Molecular Materials for Use in Fullerene-Free Organic Solar Cells. *Chem. Rec.* **2019**, *19*, 989–1007.

(31) Yuan, J.; Zhang, Y.; Zhou, L.; Zhang, G.; Yip, H.-L.; Lau, T.-K.; Lu, X.; Zhu, C.; Peng, H.; Johnson, P. A.; Leclerc, M.; Cao, Y.; Ulanski, J.; Li, Y.; Zou, Y. Single-Junction Organic Solar Cell with over 15% Efficiency Using Fused-Ring Acceptor with Electron-Deficient Core. *Joule* **2019**, *3*, 1140–1151.

(32) Cui, Y.; Yao, H.; Zhang, J.; Zhang, T.; Wang, Y.; Hong, L.; Xian, K.; Xu, B.; Zhang, S.; Peng, J.; Wei, Z.; Gao, F.; Hou, J. Over 16% Efficiency Organic Photovoltaic Cells Enabled by a Chlorinated Acceptor with Increased Open-Circuit Voltages. *Nat. Commun.* **2019**, *10*, 2515.

(33) Hou, J.; Inganäs, O.; Friend, R. H.; Gao, F. Organic Solar Cells Based on Non-Fullerene Acceptors. *Nat. Mater.* **2018**, *17*, 119–128.

(34) Baran, D.; Kirchartz, T.; Wheeler, S.; Dimitrov, S.; Abdelsamie, M.; Gorman, J.; Ashraf, R. S.; Holliday, S.; Wadsworth, A.; Gasparini, N.; Kaienburg, P.; Yan, H.; Amassian, A.; Brabec, C. J.; Durrant, J. R.; McCulloch, I. Reduced Voltage Losses Yield 10% Efficient Fullerene Free Organic Solar Cells with >1 V Open Circuit Voltages. *Energy Environ. Sci.* **2016**, *9*, 3783–3793.

(35) Bin, H.; Zhang, Z.-G.; Gao, L.; Chen, S.; Zhong, L.; Xue, L.; Yang, C.; Li, Y. Non-Fullerene Polymer Solar Cells Based on Alkylthio and Fluorine Substituted 2D-Conjugated Polymers Reach 9.5% Efficiency. *J. Am. Chem. Soc.* **2016**, *138*, 4657–4664.

(36) Kan, B.; Li, M.; Zhang, Q.; Liu, F.; Wan, X.; Wang, Y.; Ni, W.; Long, G.; Yang, X.; Feng, H.; Zuo, Y.; Zhang, M.; Huang, F.; Cao, Y.; Russell, T. P.; Chen, Y. A Series of Simple Oligomer-Like Small Molecules Based on Oligothiophenes for Solution-Processed Solar Cells with High Efficiency. *J. Am. Chem. Soc.* **2015**, *137*, 3886–3893.

(37) Lin, Y.; Wang, J.; Zhang, Z.-G.; Bai, H.; Li, Y.; Zhu, D.; Zhan, X. An Electron Acceptor Challenging Fullerenes for Efficient Polymer Solar Cells. *Adv. Mater.* **2015**, *27*, 1170–1174.

(38) Li, S.; Ye, L.; Zhao, W.; Zhang, S.; Mukherjee, S.; Ade, H.; Hou, J. Energy-Level Modulation of Small-Molecule Electron Acceptors to Achieve over 12% Efficiency in Polymer Solar Cells. *Adv. Mater.* **2016**, *28*, 9423–9429.

(39) Zhao, W.; Li, S.; Yao, H.; Zhang, S.; Zhang, Y.; Yang, B.; Hou, J. Molecular Optimization Enables over 13% Efficiency in Organic Solar Cells. *J. Am. Chem. Soc.* **2017**, *139*, 7148–7151.

(40) Holmes, N. P.; Munday, H.; Barr, M. G.; Thomsen, L.; Marcus, M. A.; Kilcoyne, A. L. D.; Fahy, A.; Stam, J. van; Dastoor, P. C.; Moons, E. Unravelling Donor–Acceptor Film Morphology Formation for Environmentally-Friendly OPV Ink Formulations. *Green Chem.* **2019**, *21*, 5090–5103.

(41) Hedley, G. J.; Ward, A. J.; Alekseev, A.; Howells, C. T.; Martins, E. R.; Serrano, L. A.; Cooke, G.; Ruseckas, A.; Samuel, I. D. W. Determining the Optimum Morphology in High-Performance Polymer-Fullerene Organic Photovoltaic Cells. *Nat. Commun.* **2013**, *4*, 2867.

(42) Sajjad, M. T.; Zhang, Y.; Geraghty, P. B.; Mitchell, V. D.; Ruseckas, A.; Blaszczyk, O.; Jones, D. J.; Samuel, I. D. W. Tailoring Exciton Diffusion and Domain Size in Photovoltaic Small Molecules by Annealing. *J. Mater. Chem. C* **2019**, *7*, 7922–7928.

(43) Tang, H.; Chen, H.; Yan, C.; Huang, J.; Fong, P. W. K.; Lv, J.; Hu, D.; Singh, R.; Kumar, M.; Xiao, Z.; Kan, Z.; Lu, S.; Li, G. Delicate Morphology Control Triggers 14.7% Efficiency All-Small-Molecule Organic Solar Cells. *Adv. Energy Mater.* **2020**, *10*, 2001076.

(44) Ge, J.; Xie, L.; Peng, R.; Fanady, B.; Huang, J.; Song, W.; Yan, T.; Zhang, W.; Ge, Z. 13.34 % Efficiency Non-Fullerene All-Small-Molecule Organic Solar Cells Enabled by Modulating the Crystallinity of Donors via a Fluorination Strategy. *Angew. Chem. Int. Ed.* **2020**, *59*, 2808–2815.

(45) He, X.; Cao, B.; Hauger, T. C.; Kang, M.; Gusarov, S.; Luber, E. J.; Buriak, J. M. Donor–Acceptor Small Molecules for Organic Photovoltaics: Single-Atom Substitution (Se or S). *ACS Appl. Mater. Interfaces* **2015**, *7*, 8188–8199.

(46) Ye, L.; Collins, B. A.; Jiao, X.; Zhao, J.; Yan, H.; Ade, H. Miscibility-Function Relations in Organic Solar Cells: Significance of Optimal Miscibility in Relation to Percolation. *Adv. Energy Mater.* **2018**, *8*, 1703058.

(47) Cheng, P.; Zhan, X. Stability of Organic Solar Cells: Challenges and Strategies. *Chem. Soc. Rev.* **2016**, *45*, 2544–2582.

(48) Zhan, C.; Yao, J. More Than Conformational “Twisting” or “Coplanarity”: Molecular Strategies for Designing High-Efficiency Nonfullerene Organic Solar Cells. *Chem. Mater.* **2016**, *28*, 1948–1964.

(49) Lee, H.; Park, C.; Sin, D. H.; Park, J. H.; Cho, K. Recent Advances in Morphology Optimization for Organic Photovoltaics. *Adv. Mater.* **2018**, *30*, 1800453.

(50) Qiu, B.; Chen, Z.; Qin, S.; Yao, J.; Huang, W.; Meng, L.; Zhu, H.; Yang, Y.; Zhang, Z.-G.; Li, Y. Highly Efficient All-Small-Molecule Organic Solar Cells with Appropriate Active Layer Morphology by Side Chain Engineering of Donor Molecules and Thermal Annealing. *Adv. Mater.* **2020**, *32*, 1908373.

(51) Min, J.; Güldal, N. S.; Guo, J.; Fang, C.; Jiao, X.; Hu, H.; Heumüller, T.; Ade, H.; Brabec, C. J. Gaining Further Insight into the Effects of Thermal Annealing and Solvent Vapor Annealing on Time Morphological Development and Degradation in Small Molecule Solar Cells. *J. Mater. Chem. A* **2017**, *5*, 18101–18110.

(52) Zomerman, D.; Kong, J.; McAfee, S. M.; Welch, G. C.; Kelly, T. L. Control and Characterization of Organic Solar Cell Morphology Through Variable-Pressure Solvent Vapor Annealing. *ACS Appl. Energy Mater.* **2018**, *1*, 5663–5674.

(53) Engmann, S.; Ro, H. W.; Herzing, A.; Snyder, C. R.; Richter, L. J.; Geraghty, P. B.; Jones, D. J. Film Morphology Evolution During Solvent Vapor Annealing of Highly Efficient Small Molecule Donor/Acceptor Blends. *J. Mater. Chem. A* **2016**, *4*, 15511–15521.

(54) Kan, B.; Feng, H.; Wan, X.; Liu, F.; Ke, X.; Wang, Y.; Wang, Y.; Zhang, H.; Li, C.; Hou, J.; Chen, Y. Small-Molecule Acceptor Based on the Heptacyclic Benzodi(Cyclopentadithiophene) Unit for Highly Efficient Nonfullerene Organic Solar Cells. *J. Am. Chem. Soc.* **2017**, *139*, 4929–4934.

(55) McDowell, C.; Abdelsamie, M.; Toney, M. F.; Bazan, G. C. Solvent Additives: Key Morphology-Directing Agents for Solution-Processed Organic Solar Cells. *Adv. Mater.* **2018**, *30*, 1707114.

(56) Gao, K.; Jo, S. B.; Shi, X.; Nian, L.; Zhang, M.; Kan, Y.; Lin, F.; Kan, B.; Xu, B.; Rong, Q.; Shui, L.; Liu, F.; Peng, X.; Zhou, G.; Cao, Y.; Jen, A. K. Over 12% Efficiency Nonfullerene All-Small-Molecule Organic Solar Cells with Sequentially Evolved Multilength Scale Morphologies. *Adv. Mater.* **2019**, *31*, 1807842.

(57) Sun, C.; Pan, F.; Bin, H.; Zhang, J.; Xue, L.; Qiu, B.; Wei, Z.; Zhang, Z.-G.; Li, Y. A Low Cost and High Performance Polymer Donor Material for Polymer Solar Cells. *Nat. Commun.* **2018**, *9*.

(58) Leardi, R. Experimental Design in Chemistry: A Tutorial. *Anal. Chim. Acta* **2009**, *652*, 161–172.

(59) Jia, X.; Lynch, A.; Huang, Y.; Danielson, M.; Lang'at, I.; Milder, A.; Ruby, A. E.; Wang, H.; Friedler, S. A.; Norquist, A. J.; Schrier, J. Anthropogenic Biases in Chemical Reaction Data Hinder Exploratory Inorganic Synthesis. *Nature* **2019**, *573*, 251–255.

(60) Cao, B.; Adutwum, L. A.; Oliynyk, A. O.; Luber, E. J.; Olsen, B. C.; Mar, A.; Buriak, J. M. How to Optimize Materials and Devices *via* Design of Experiments and Machine Learning: Demonstration Using Organic Photovoltaics. *ACS Nano* **2018**, *12*, 7434–7444.

(61) Lee, M.-H. Insights from Machine Learning Techniques for Predicting the Efficiency of Fullerene Derivatives-Based Ternary Organic Solar Cells at Ternary Blend Design. *Adv. Energy Mater.* **2019**, *9*, 1900891.

(62) Sun, W.; Zheng, Y.; Yang, K.; Zhang, Q.; Shah, A. A.; Wu, Z.; Sun, Y.; Feng, L.; Chen, D.; Xiao, Z.; Lu, S.; Li, Y.; Sun, K. Machine Learning–Assisted Molecular Design and Efficiency Prediction for High-Performance Organic Photovoltaic Materials. *Sci. Adv.* **2019**, *5*, eaay4275.

(63) Padula, D.; Simpson, J. D.; Troisi, A. Combining Electronic and Structural Features in Machine Learning Models to Predict Organic Solar Cells Properties. *Mater. Horiz.* **2019**, *6*, 343–349.

(64) Lopez, S. A.; Sanchez-Lengeling, B.; Soares, J. de G.; Aspuru-Guzik, A. Design Principles and Top Non-Fullerene Acceptor Candidates for Organic Photovoltaics. *Joule* **2017**, *1*, 857–870.

(65) Brown, K. A.; Brittman, S.; Maccaferri, N.; Jariwala, D.; Celano, U. Machine Learning in Nanoscience: Big Data at Small Scales. *Nano Lett.* **2020**, *20*, 2–10.

(66) MacLeod, B. P.; Parlane, F. G. L.; Morrissey, T. D.; Häse, F.; Roch, L. M.; Dettelbach, K. E.; Moreira, R.; Yunker, L. P. E.; Rooney, M. B.; Deeth, J. R.; Lai, V.; Ng, G. J.; Situ, H.; Zhang, R. H.; Elliott, M. S.; Haley, T. H.; Dvorak, D. J.; Aspuru-Guzik, A.; Hein, J. E.; Berlinguette, C. P. Self-Driving Laboratory for Accelerated Discovery of Thin-Film Materials. *Sci. Adv.* **2020**, *6*, eaaz8867.

(67) Mora-Tamez, L.; Barim, G.; Downes, C.; Williamson, E. M.; Habas, S. E.; Brutchey, R. L. Controlled Design of Phase- and Size-Tunable Monodisperse Ni2P Nanoparticles in a Phosphonium-Based Ionic Liquid Through Response Surface Methodology. *Chem. Mater.* **2019**, *31*, 1552–1560.

(68) Voznyy, O.; Levina, L.; Fan, J. Z.; Askerka, M.; Jain, A.; Choi, M.-J.; Ouellette, O.; Todorović, P.; Sagar, L. K.; Sargent, E. H. Machine Learning Accelerates Discovery of Optimal Colloidal Quantum Dot Synthesis. *ACS Nano* **2019**, *13*, 11122–11128.

(69) Wei, L.; Xu, X.; Gurudayal; Bullock, J.; Ager, J. W. Machine Learning Optimization of P-Type Transparent Conducting Films. *Chem. Mater.* **2019**, *31*, 7340–7350.

(70) Häse, F.; Roch, L. M.; Kreisbeck, C.; Aspuru-Guzik, A. Phoenics: A Bayesian Optimizer for Chemistry. *ACS Cent. Sci.* **2018**, *4*, 1134–1145.

(71) Sun, Y.; Seo, J. H.; Takacs, C. J.; Seifter, J.; Heeger, A. J. Inverted Polymer Solar Cells Integrated with a Low-Temperature-Annealed Sol-Gel-Derived ZnO Film as an Electron Transport Layer. *Adv. Mater.* **2011**, *23*, 1679–1683.

(72) Nečas, D.; Klapetek, P. Gwyddion: An Open-Source Software for SPM Data Analysis. *Cent. Eur. J. Phys.* **2012**, *10*, 181–188.

(73) Ge, J.; Wei, Q.; Peng, R.; Zhou, E.; Yan, T.; Song, W.; Zhang, W.; Zhang, X.; Jiang, S.; Ge, Z. Improved Efficiency in All-Small-Molecule Organic Solar Cells with Ternary Blend of Nonfullerene Acceptor and Chlorinated and Nonchlorinated Donors. *ACS Appl. Mater. Interfaces* **2019**, *11*, 44528–44535.

(74) Qiu, B.; Xue, L.; Yang, Y.; Bin, H.; Zhang, Y.; Zhang, C.; Xiao, M.; Park, K.; Morrison, W.; Zhang, Z.-G.; Li, Y. All-Small-Molecule Nonfullerene Organic Solar Cells with High Fill Factor and High Efficiency over 10%. *Chem. Mater.* **2017**, *29*, 7543–7553.

(75) Wang, J.-C.; Weng, W.-T.; Tsai, M.-Y.; Lee, M.-K.; Horng, S.-F.; Perng, T.-P.; Kei, C.-C.; Yu, C.-C.; Meng, H.-F. Highly Efficient Flexible Inverted Organic Solar Cells Using Atomic Layer Deposited ZnO as Electron Selective Layer. *J. Mater. Chem.* **2010**, *20*, 862–866.

(76) Daughton, W. J. An Investigation of the Thickness Variation of Spun-on Thin Films Commonly Associated with the Semiconductor Industry. *J. Electrochem. Soc.* **1982**, *129*, 173.

(77) Surowiec, I.; Vikström, L.; Hector, G.; Johansson, E.; Vikström, C.; Trygg, J. Generalized Subset Designs in Analytical Chemistry. *Anal. Chem.* **2017**, *89*, 6491–6497.

(78) Brabec, C. J.; Cravino, A.; Meissner, D.; Sariciftci, N. S.; Fromherz, T.; Rispens, M. T.; Sanchez, L.; Hummelen, J. C. Origin of the Open Circuit Voltage of Plastic Solar Cells. *Adv. Funct. Mater.* **2001**, No. 5, 7.

(79) Cnops, K.; Zango, G.; Genoe, J.; Heremans, P.; Martinez-Diaz, M. V.; Torres, T.; Cheyns, D. Energy Level Tuning of Non-Fullerene Acceptors in Organic Solar Cells. *J. Am. Chem. Soc.* **2015**, *137*, 8991–8997.

(80) Li, H.; Zhao, Y.; Fang, J.; Zhu, X.; Xia, B.; Lu, K.; Wang, Z.; Zhang, J.; Guo, X.; Wei, Z. Improve the Performance of the All-Small-Molecule Nonfullerene Organic Solar Cells Through Enhancing the Crystallinity of Acceptors. *Adv. Energy Mater.* **2018**, *8*, 1702377.

(81) Yu, L.; Qian, D.; Marina, S.; Nugroho, F. A. A.; Sharma, A.; Hultmark, S.; Hofmann, A. I.; Kroon, R.; Benduhn, J.; Smilgies, D.-M.; Vandewal, K.; Andersson, M. R.; Langhammer, C.; Martín, J.; Gao, F.; Müller, C. Diffusion-Limited Crystallization: A Rationale for the Thermal Stability of Non-Fullerene Solar Cells. *ACS Appl. Mater. Interfaces* **2019**, *11*, 21766–21774.

(82) Shi, S.; Yuan, J.; Ding, G.; Ford, M.; Lu, K.; Shi, G.; Sun, J.; Ling, X.; Li, Y.; Ma, W. Improved All-Polymer Solar Cell Performance by Using Matched Polymer Acceptor. *Adv. Funct. Mater.* **2016**, *26*, 5669–5678.